International Journal of Heat and Fluid Flow 108 (2024) 109444

Contents lists available at ScienceDirect

International Journal of Heat and Fluid Flow

journal homepage: www.elsevier.com/locate/ijhff

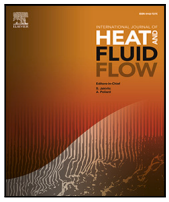

Skin friction reduction via suppression of large scales in turbulent Couette flows

A. Andreolli *, M.K. Singh, D. Gatti

Institute of Fluid Mechanics, Karlsruhe Institute of Technology, Karlsruhe, DE-76131, Germany

ARTICLE INFO

Keywords:
Turbulent wall-bounded flow
Large-scale structure
Flow control
Drag reduction

ABSTRACT

We investigate the drag-reduction achieved by suppressing the Very-Large-Scale Motion (VLSM) that is typical of turbulent Couette flows. A weak Coriolis force is used for this purpose, as pioneered by Komminaho et al. (1996). The main advantage of this strategy is that it only suppresses the VLSM without suppressing other motions of similar scale. The suppression effect is though progressive with the intensity of the Coriolis force, and direct effects of the forcing on the small scales are hard to isolate, albeit marginal. At the highest Reynolds number investigated, we observe a 13% drag reduction at constant flow rate, suggesting that significant savings can be achieved by controlling large scales when they are particularly intense (at high Reynolds numbers). Performance gains yielded by the suppression of the VLSM are partially compensated by a higher-than-expected contribution to the skin friction from smaller (yet not necessarily small) scales, as measured using the Constant Power Input (CPI) framework (Gatti et al., 2018) . The analysis of energy spectra suggests that these unexpected expenses are caused by the energisation of outer-scaled eddies residing near the centreline of the channel. We also argue that the CPI framework is better suited than the FIK identity to measure the skin friction contribution of small and large scales. Finally, we discuss the analogy between the currently used Coriolis force and other feedback control strategies.

1. Introduction

The energy spectrum of turbulent flows is notoriously continuous, meaning that turbulence comprises eddies of virtually any size (Davidson, 2015). However, in the buffer layer of a wall-bounded flow (that is, at a distance of roughly $10\,\delta_v$ from the wall, where δ_v is the viscous or inner length) one is most likely to observe turbulent features with a spanwise spacing of roughly $100\,\delta_v$ (Kline et al., 1967; Kim et al., 1987). These are commonly referred to as small scales and their energy is known to scale with the friction velocity $u_\tau = \sqrt{\tau_w/\rho}$ (τ_w being the wall shear stress and ρ the density; see Hoyas and Jiménez, 2006; Marusic et al., 2010). Additionally, small scales are known to self-sustain through the near-wall cycle (Jiménez and Moin, 1991; Jiménez and Pinelli, 1999; Panton, 2001). On the other hand, one is most likely to encounter larger flow features in the outer-layer as long as the Reynolds number is sufficiently high (Kim and Adrian, 1999; Hutchins and Marusic, 2007a; Lee and Moser, 2018). The size of these outer-layer motions is flow dependent and scales with some outer variables (for instance, the half channel height h in a channel flow). Outer-scaled motions are usually further categorised into Large- (LSMs) and Very-Large-Scale Motions (VLSMs) depending on their streamwise extent (Kim and Adrian, 1999); in the following, the term "large" is used to indicate an outer-scaled motion (which could be a LSM or a VLSM), whereas the acronyms are used to indicate the two separate categories. LSMs typically have an extent of $2-3h$ (Kim and Adrian, 1999; Balakumar and Adrian, 2007; Monty et al., 2009), where h could represent the channel half-height (as in the present paper), the pipe radius or the boundary layer thickness depending on the considered flow. VLSMs instead are defined as having a longer ($> 3h$, see Balakumar and Adrian, 2007) streamwise extent. It has also been proposed that LSMs would ensue from the agglomeration of hairpin vortices (Kim and Adrian, 1999; Zhou et al., 1999), whereas VLSMs would result from the coherent alignment of LSMs (Kim and Adrian, 1999). Nevertheless, the mechanism through which h-scaled motions originate and self-sustain is still object of research (Iwamoto et al., 2004; Toh and Itano, 2005; Del Álamo and Jiménez, 2006; Hwang and Cossu, 2010; de Giovanetti et al., 2017; Lee and Moser, 2019; Illingworth, 2020; Zhou et al., 2022). In spite of this dichotomy between outer- and inner-scaled features, a considerable share of the energy of a turbulent flow is contained by vortices of intermediate size extending from the wall up to a given wall-normal height, the so-called attached eddies (Marusic and Perry, 1995; Hwang, 2015; Baars and Marusic, 2020; Puccioni et al., 2023).

* Corresponding author.
E-mail address: a.andreolli@kit.edu (A. Andreolli).

https://doi.org/10.1016/j.ijheatfluidflow.2024.109444
Received 23 December 2023; Received in revised form 19 April 2024; Accepted 27 May 2024
Available online 4 June 2024

Notice that the size of attached eddies can actually overlap with that of outer-scaled motions.

The presence of all these vortices of different sizes contributes to momentum mixing, which in turn results in an increase (with respect to a laminar flow) of the drag force felt at the wall — the so-called turbulent skin-friction drag. Many strategies have been proposed to achieve turbulent skin friction reduction by either controlling small or large features of wall-bounded turbulent flows; so far, targeting small scales has been the more successful and better understood strategy (for instance, Walsh et al., 1989; Karniadakis and Choi, 2003; Quadrio and Ricco, 2004; Quadrio et al., 2009; Kasagi et al., 2009). However, this approach loses performance with increasing Reynolds number (though a substantial drag reduction should be achievable also at Reynolds numbers of practical interests; see Iwamoto et al., 2005; Gatti and Quadrio, 2016). Most crucially, it requires miniaturisation of the controlling actuators as the size of near-wall eddies becomes smaller with increasing Reynolds number, hindering practical feasibility; examples of the miniaturisation effort can be found in the review by Kasagi et al. (2009).

In light of the two above issues, large-scale control has become of interest. The first approach in chronological order has been to numerically superpose large-scaled vortices to near-wall turbulence; the original work by Schoppa and Hussain (1998) has been followed by a series of studies (Canton et al., 2016a,b; Yao et al., 2017) highlighting (and proposing solutions to) a loss of performance with increasing Reynolds number. More recently, large-scale control has been experimentally pursued through strategies originally developed for small scales, namely spanwise oscillations of the wall (Marusic et al., 2021) and opposition control (Abbassi et al., 2017; Ibrahim et al., 2020). The latter scheme was originally proposed by Choi et al. (1994) and consists in sensing large-scale ejection and (or) sweep events at the wall and opposing them through suction and (or) blowing respectively.

Alongside these experimental approaches, which to the authors' knowledge only lead to a modest reduction of the spectral energy of the large structures, it has also been attempted to numerically quantify the impact of large scales on the skin friction, and consequently the drag reduction potentially achievable through their complete removal. For instance, one can analyse some turbulent flow in presence of large scales; identities such as the FIK (Fukagata et al., 2002) and the Renard–Deck (RD, Renard and Deck, 2016) ones can be used to link turbulent fluctuations to the wall shear stress. Then, turbulent fluctuations can be decomposed into their large- and small-scale contributions through low-pass filtering. The result of the process is the share of skin friction caused by large scales. This approach has been pursued, for example, by Deck et al. (2014), de Giovanetti et al. (2016) and Agostini and Leschziner (2018). Using a similar procedure, we have shown in a previous work (Andreolli et al., 2021) that large scales tend to induce energy waste (closely related to drag) in the form of deviations of the mean flow from its ideal profile, rather than in the form of turbulent dissipation. However, the whole procedure described above suffers from arbitrariness in the choice of filter and decomposition (FIK or RD); in particular, results are not robust to the choice of the latter (Agostini and Leschziner, 2019). Additionally, the so-calculated share of skin friction contributed by large scales is not necessarily representative of the drag reduction arising from their removal, as nonlinearities can alter the observed change in skin friction.

To account for non-linear effects, one can then numerically suppress the large scales and measure the obtained drag reduction. Fukagata et al. (2010) used modal damping to suppress large-scale wall-normal fluctuations, obtaining indeed drag reduction, but also observing an increase of the small-scale contribution to skin friction. Similarly, de Giovanetti et al. (2016) compared the drag reduction obtained by artificially removing large scales from a channel flow and the one predicted by the FIK identity by excluding the large-scale Reynolds shear stress contribution in the original flow; they found that the predicted drag reduction exceeds the measured one, attributing this discrepancy to non-linear scale interactions that arise when large scales are physically removed. The latter authors also resorted to modal damping for the removal of large structures; additionally, following Hwang (2013), they removed the structures by restricting the spanwise simulation domain. By doing so, large scales are aliased on a spanwise-invariant mode, so that an additional correction term is needed for their complete removal (as reported by the authors).

Wall-bounded turbulent flows are known to be sensitive to a weak spanwise rotation of the reference frame, which can either stabilise or destabilise the flow — meaning that the fluctuation intensities and turbulent production are either decreased or increased, as well as the wall-layer streak bursting rate (Johnston et al., 1972). The effect of the rotation is determined by the ratio $S(y) = -2\Omega/(\mathrm{d}U/\mathrm{d}y)$ between the angular velocity Ω of the reference frame and the spanwise flow vorticity $\bar{\omega}_z = -\mathrm{d}U/\mathrm{d}y$, where U is the mean streamwise velocity and y the wall-normal coordinate (Johnston et al., 1972). A cyclonic rotation of the reference frame – that is, one where Ω and $\bar{\omega}_z$ have the same sign, hence $S > 0$ – always locally stabilises the flow. An anticyclonic rotation (when Ω and $\bar{\omega}_z$ have the same sign, $S < 0$) is instead locally destabilising as long as $|S| < 1$.

The (de-)stabilising action is mainly provided by the Coriolis force in a similar way to how a temperature (or density) gradient can stabilise or destabilise a buoyancy-driven flow (Lezius and Johnston, 1976; Tritton, 1992; Komminaho et al., 1996). The effects of the Coriolis force are most easily observed in a plane Couette flow, where the vorticity $\bar{\omega}_z$ has the same sign across the channel height, meaning that the Coriolis force has a stabilising or destabilising effect across the entire channel. By contrast, a plane Poiseuille (or, simply, channel) flow has different signs of the vorticity at the two walls, meaning that one side of the channel is stabilised by rotation, whereas the other is destabilised (Kristoffersen and Andersson, 1993). Rotating plane Couette flows have been studied (Bech and Andersson, 1996; Tillmark and Alfredsson, 1996; Kawata and Alfredsson, 2016, 2019) in both stabilising and destabilising configurations; a comprehensive description of the flow regimes obtained with varying Reynolds number and angular velocity is provided by Tsukahara et al. (2010). The destabilised configuration has been more thoroughly investigated owing to the counter-rotating roll cells that can be observed in such conditions. Such roll cells closely resemble, but differ from Tsukahara et al. (2010) the naturally occurring rolling motion (Pirozzoli et al., 2014; Lee and Moser, 2018) that can be observed in Couette flows without rotation. For clarity's sake, we will refer to the latter, naturally occurring rolling motion as "the VLSM": its streamwise extent ($20 - 100h$ and more, see Lee and Moser, 2018; Gandía-Barberá et al., 2018) far exceeds the typical threshold of $3h$ (Balakumar and Adrian, 2007) used to discriminate LSMs and VLSMs.

The less investigated stabilising regime of the Coriolis force is of interest for this study: it has been shown both experimentally (Tsukahara et al., 2010) and numerically (Komminaho et al., 1996) that a weak stabilising Coriolis force can remove the VLSM from the flow. The latter authors went on to compare a natural Couette flow with one where the VLSM is suppressed; since the small-scales are minimally affected, they were able to estimate the contribution of the VLSM to the turbulent kinetic energy. Yet, this was done at an almost transitional Reynolds number, and a parametric study on the intensity of the Coriolis force needed to yield a satisfactory suppression of the VLSM with minimal intrusiveness is missing.

In this paper, we revisit the VLSM-suppressing technique of Komminaho et al. (1996) as a flow control strategy in Couette flows at higher Reynolds numbers and with changing intensity of the Coriolis force. As explained above, previous studies (e.g., Fukagata et al., 2010; de Giovanetti et al., 2016) have highlighted that the removal of large scales results in non-trivial nonlinear effects, which we investigate using the Constant Power Input framework (CPI, see Gatti et al., 2018; Andreolli et al., 2021). In Section 2 we present our numerical methods and flow configuration; in Section 3.1 we discuss the degree of suppression of the

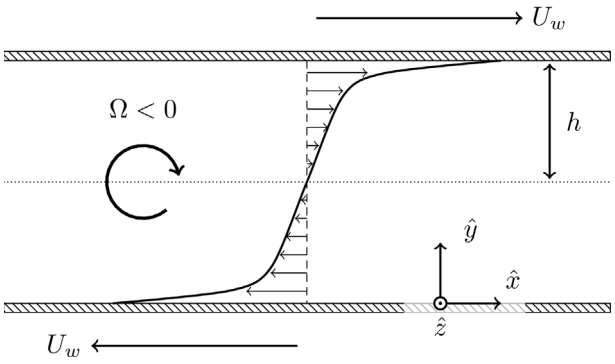

Fig. 1. A schematic representation of the considered flow.

VLSM with increasing control intensity as well as the intrusiveness on small scales. In Section 3.2 we briefly discuss the CPI framework and how it differs from the FIK identity; we then use it in Section 3.3 to assess the impact of the Coriolis force on the flow. A discussion of the obtained drag reduction is also provided. In Section 4 we discuss how the Coriolis force achieves the suppression; we argue that it works in a similar way to the feedback control of Fukagata et al. (2005). Finally, Section 5 presents a concluding remark.

2. Problem description and numerical details

We perform direct numerical simulations of turbulent plane Couette flows using the solver described in Luchini and Quadrio (2006). The flow is schematically depicted in Fig. 1. The two parallel indefinite walls of the channel move in opposite directions at the same speed U_w. The $\hat{x}$ unit vector indicates the streamwise direction and is defined so that the bottom wall has a negative velocity. The $\hat{y}$ one is oriented in the wall-normal direction and $\hat{z}$ is consequently defined to be the spanwise one. Axes are denoted by the same letters without hat; the bottom wall is located at $y = 0$.

The system is subject to the Coriolis body force $\vec{f}_c$ that would be given by a rotation of the reference system about the spanwise axis:

$$\vec{f}_c = -2\rho\,\Omega\hat{z}\times\vec{u}, \tag{1}$$

where ρ is the uniform density of the fluid. The direction of rotation is cyclonic, meaning that the angular velocity Ω has the same sign of the mean vorticity $\bar{\omega}_z$ of the flow ($\Omega < 0$ as $\bar{\omega}_z < 0$). Notice that the Coriolis force is orthogonal to the velocity field $\vec{u}$ by definition; hence it cannot provide nor subtract energy to the flow.

After making them dimensionless with the channel half height h and the speed of the walls U_w, which defines a Reynolds number $Re_w = hU_w/\nu$ (ν being the kinematic viscosity), the governing equations read:

$$\nabla_o\cdot\vec{u}_o = 0 \tag{2}$$

$$\frac{\partial\vec{u}_o}{\partial t_o} + (\vec{u}_o\cdot\nabla_o)\vec{u}_o + \nabla_o P_o = \frac{1}{Re_w}\nabla_o^2\vec{u}_o - \underbrace{2\frac{\Omega h}{U_w}}_{Ro}\hat{z}\times\vec{u}_o \tag{3}$$

where the $(\cdot)_o$ subscript indicates quantities made dimensionless with outer units (h, U_w), $\vec{u}$ is the velocity vector with its streamwise, wall-normal and spanwise components (u, v, w) and P the pressure; $\times$ indicates a vector product. In addition to the Reynolds number, a second dimensionless group appears in the equations, that is, the rotation number $Ro = 2\Omega h/U_w$ (Lezius and Johnston, 1976) governing the relative intensity of the Coriolis force.

The control intensity Ro is progressively increased as the Reynolds number Re_w is kept constant; this is equivalent to performing a parametric analysis at constant flow rate (CFR), since Re_w represents an analogue of the bulk Reynolds number in a Couette flow (Andreolli et al., 2021). This is done at a low and at a moderate Reynolds number, corresponding to a friction Reynolds number $Re_\tau = hu_\tau/\nu$ of roughly 100 and 500 respectively when no control is applied. Data for uncontrolled Couette flows are taken from simulations of Andreolli et al. (2021), who used a wide enough box size to accommodate the VLSM and a standard resolution. The same mesh is used for the controlled cases; this choice is suited as the suppression of the VLSM and the consequent drag reduction relieve the constraints on both the box size and the resolution. A summary of the numerical details is provided in Table 1.

Table 1
Numerical details for the present numerical dataset. Here, N_f represents the number of snapshots acquired at a statistically steady state for the calculation of statistics; the spacing between snapshots is of roughly $1\,h/u_\tau$ (except for the simulations at $Ro = 0$, which are taken from Andreolli et al., 2021). L_x and L_z represent the simulation domain length in the stream- and span-wise directions respectively; the grid spacing is uniform in these directions and is represented by Δx and Δz. As for the wall-normal direction, Δy_w and Δy_c represent the spacing at the wall and centreline respectively.

Re_w	Ro	Re_τ	N_f	L_x/h	L_z/h	Δx^+	Δz^+	Δy_w^+	Δy_c^+
1667	0	101.7	408	12π	4π	10.0	5.0	0.5	2.6
1667	$-2\cdot10^{-3}$	100.8	250	12π	4π	9.9	4.9	0.5	2.6
1667	$-5\cdot10^{-3}$	99.5	250	12π	4π	9.8	4.9	0.5	2.6
1667	$-1\cdot10^{-2}$	97.3	250	12π	4π	9.6	4.8	0.5	2.5
1667	$-2\cdot10^{-2}$	92.5	250	12π	4π	9.1	4.5	0.4	2.4
1667	$-3\cdot10^{-2}$	86.5	250	12π	4π	8.5	4.2	0.4	2.2
10 133	0	507.1	223	16π	8π	12.5	6.2	1.0	7.2
10 133	$-5\cdot10^{-3}$	473.4	150	16π	8π	11.6	5.8	0.9	6.8
10 133	$-1\cdot10^{-2}$	457.8	150	16π	8π	11.2	5.6	0.9	6.5
10 133	$-2\cdot10^{-2}$	435.1	150	16π	8π	10.7	5.3	0.8	6.2

As for the notation used in this manuscript, a $(\cdot)^+$ superscript indicates quantities made dimensionless with inner units (δ_v, u_τ). Averaging in time and in the spatial homogeneous directions is indicated by $\langle\cdot\rangle$. Such an averaging operator can be used to define the usual Reynolds decomposition of the velocity $\vec{u}$ (and similarly of other flow quantities):

$$\vec{u} = \langle\vec{u}\rangle + \vec{u}', \tag{4}$$

where $\langle\vec{u}\rangle = U\hat{x}$ is the mean velocity and only has a non-zero streamwise component U. The remaining term $\vec{u}'$ indicates velocity fluctuations instead.

3. Results

3.1. Mean velocity, spectra and VLSM suppression

In this section, we show basic flow statistics and discuss how the VLSM is suppressed with increasing rotation number; effects on small scales are also discussed. First off, we inspect how the Coriolis force affects the mean velocity profile in Fig. 2 for all available simulations. Notice that Fig. 2 compensates for the fact that both walls have a non-zero velocity in our numerical setup. The usual collapse of the inner-scaled velocity profile is seen in the near-wall region, indicating that the control force does not substantially alter the near-wall dynamics. Deviations of the mean velocity profiles from the uncontrolled case are seen only towards the centreline: there, larger absolute values of the rotation number Ro are associated to larger values of the inner-scaled velocity. This could be a symptom of drag reduction; a thorough discussion of the matter will be given in Section 3.3.

The presence of the VLSM in Couette flows is usually revealed by analysing velocity spectra or visually inspecting flow snapshots (Lee and Moser, 2018). The VLSM is indeed easily observable without further postprocessing of the acquired data, although a short-time average or a long-exposure picture may help (see, for instance, Tsukahara et al., 2010). We begin by comparing two flow snapshots at $Re_\tau \approx 500$: one from an uncontrolled simulation and one subject to the Coriolis force with a given value of the rotation number ($Ro = -10^{-2}$). This is done to

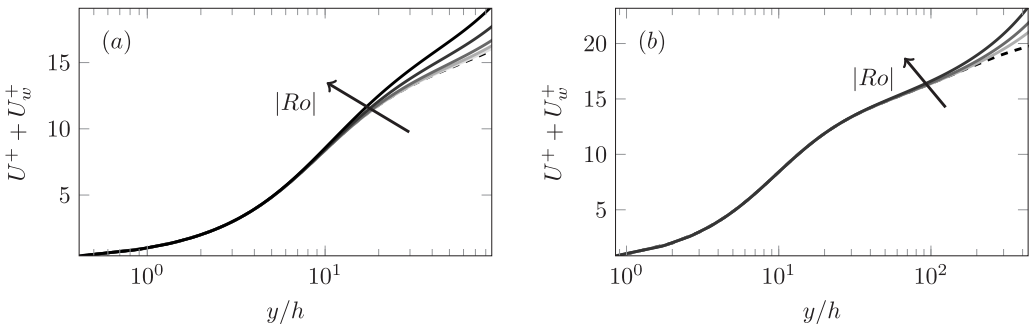

Fig. 2. Inner-scaled mean velocity profile $U^+(y^+) + U_w^+$ for all available simulations (see Table 1), adjusting for the velocity of the bottom wall. The dashed lines indicate $Ro = 0$; otherwise, darker shades of grey indicate a larger absolute value of Ro. (a) $Re_\tau \approx 100$; (b) $Re_\tau \approx 500$.

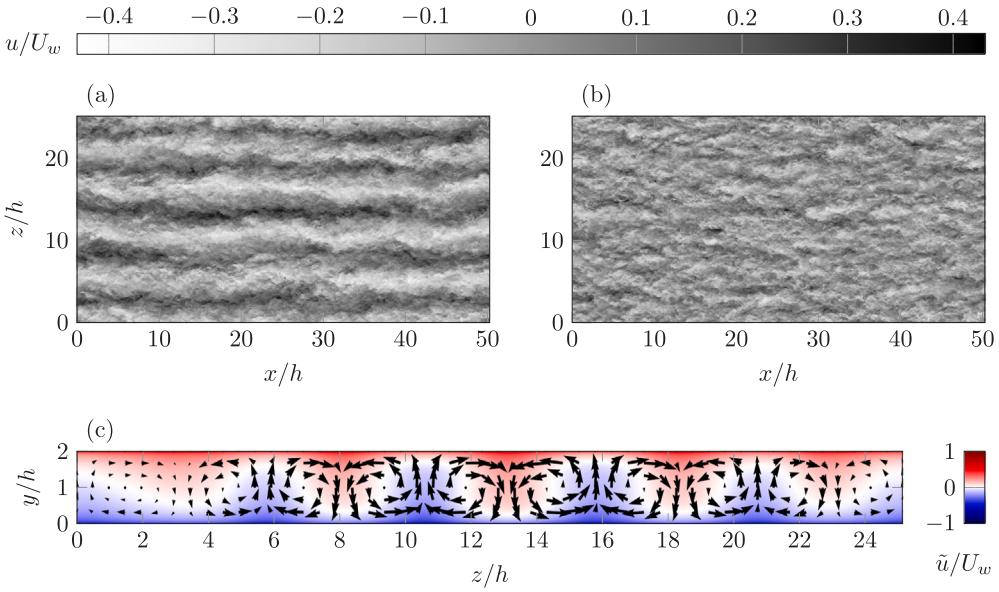

Fig. 3. Instantaneous visualisations of the streamwise velocity u at the centreline ($y/h = 1$); $Re_\tau \approx 500$, $Ro = 0$ (a) and $Ro = -10^{-2}$ (b). Cross-sectional view of the streamwise- and time-averaged velocity field (c); $Re_\tau \approx 500$, $Ro = 0$. The colour indicates the streamwise component $\tilde{u}$; the two remaining components are represented as vectors. (For interpretation of the references to colour in this figure legend, the reader is referred to the web version of this article.)

show both the appearance of the VLSM and the effects of the Coriolis force in physical space; a more thorough discussion of the VLSM-suppression is presented later. Fig. 3(a–b) shows the instantaneous distribution of streamwise velocity at the midplane for the two selected flow cases. In the uncontrolled one, streamwise-coherent regions of low and high momentum can be clearly distinguished; they repeat themselves quasi-periodically in the spanwise direction with a period of roughly $5h$. These high- and low-momentum streaks are the most easily indentifiable feature of the VLSM (Pirozzoli et al., 2014; Lee and Moser, 2018); they disappear when the Coriolis force is applied, suggesting that the VLSM is being suppressed. Following Lee and Moser (2018), an averaged visualisation of the VLSM can be produced by exploiting its extended streamwise and time coherence. We average the velocity field of the uncontrolled simulation in the streamwise direction as well as in time (using all saved snapshots, which span a time window of $2220\,h/U_w$). The result is shown in Fig. 3(c), revealing the presence of quasi-periodically repeating pairs of counter-rotating vortices extending from one wall to the other. Neighbouring vortices induce regions of upwelling and downwelling motion where low- and high-momentum fluid is pulled away from the bottom and top walls respectively, so that the streaks seen in Fig. 3(a) are formed.

To better investigate the VLSM-suppression, we analyse the spectra of both controlled and uncontrolled flows. Fig. 4 shows the spanwise (co-)spectra for each of the nonzero Reynolds stresses for the uncontrolled and a selected controlled Couette flow at $Re_\tau \approx 500$. The remaining cases are not shown for conciseness and return the same qualitative picture described here. The uncontrolled case features a spectral peak around a spanwise wavelength of $\lambda_z/h = 5$ for each component of the Reynolds stress tensor. This is the spectral representation of the streaky structure seen in Fig. 3(a); it has also been observed, for instance, by Lee and Moser (2018). The main effect of the applied forcing is the disappearance of this spectral peak for all components of the Reynolds stress tensor; otherwise, all (co-)spectra maintain the qualitative structure of the uncontrolled case. The only other noticeable difference is a moderate increase in the fluctuation energy at the centreline; this is particularly relevant for the Reynolds shear stress, which receives at $y/h \approx 1$ an increased contribution from motions that are outer-scaled ($\lambda_z/h \approx 2$), yet smaller than the VLSM.

This shows that the main effect of the application of a weak Coriolis force to a Couette flow is the suppression of the VLSM, accompanied by a modest increase in the energy of large, non-VLSM eddies; further effects on the remaining scales of motion will be discussed at the end of this section. One advantage of the Coriolis force approach with respect to modal damping or spanwise domain restriction (used, for instance, by de Giovanetti et al., 2016) is that the former does not suppress the large-scaled motions (possibly attached eddies) coexisting

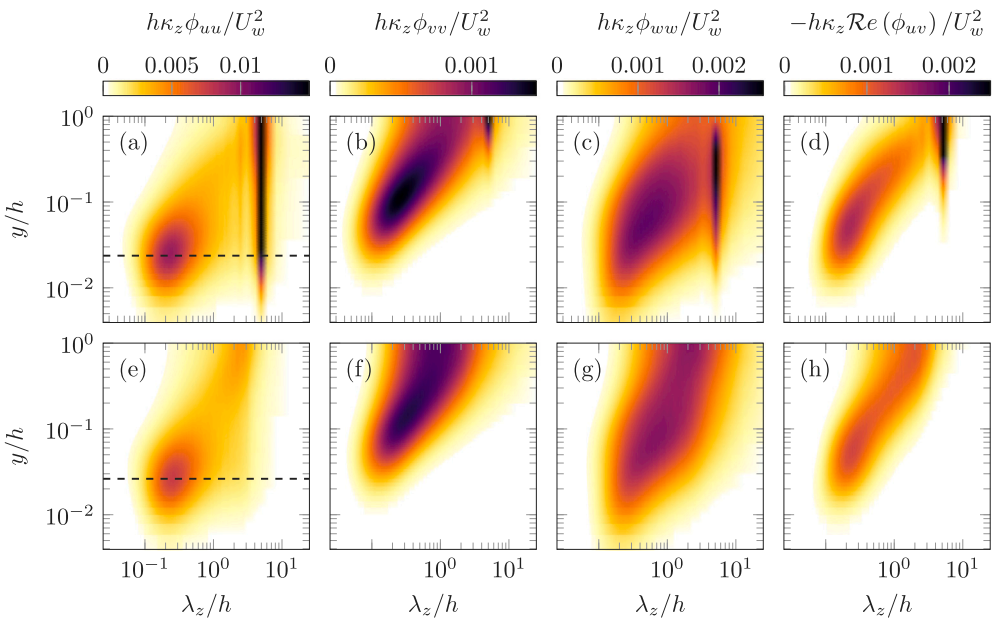

Fig. 4. Premultiplied one-dimensional spanwise (co-)spectra $\kappa_z\boldsymbol{\Phi}_{uu}$, $\kappa_z\boldsymbol{\Phi}_{vv}$, $\kappa_z\boldsymbol{\Phi}_{ww}$, $-\kappa_z\mathcal{R}e\left(\boldsymbol{\Phi}_{uv}\right)$ ($\mathcal{R}e$ indicating the real part of a complex number) of the non-zero Reynolds stress tensor components; streamwise, wall-normal and spanwise normal stresses and shear stress respectively. (a-d) $Re_\tau \approx 500$, $Ro = 0$; (e-h) $Re_\tau \approx 500$, $Ro = -10^{-2}$. The dashed lines in panels (a), (e) indicate the inner-layer wall-normal position ($y^+ = 12$) at which the spectrum is re-analysed in Fig. 7.

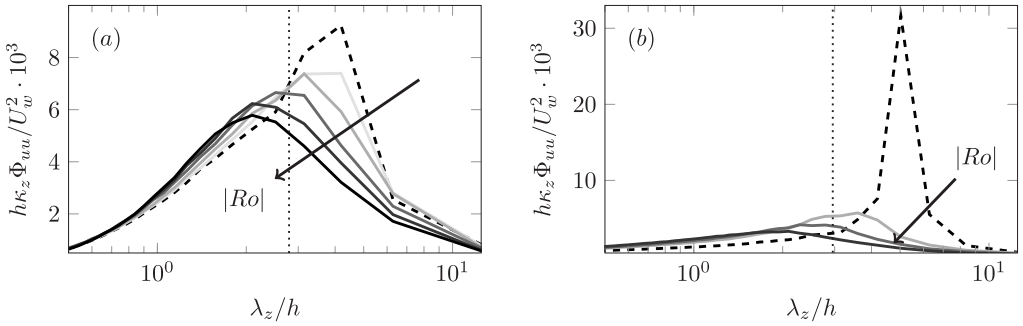

Fig. 5. Premultiplied one-dimensional spanwise spectrum $\kappa_z\boldsymbol{\Phi}_{uu}$ of the streamwise fluctuations for changing value of the control intensity $|Ro|$ at the midplane ($y/h = 1$); (a) $Re_\tau \approx 100$ and (b) $Re_\tau \approx 500$. The dashed lines indicate $Ro = 0$; as for the solid lines, darker shades indicate an increasing magnitude of Ro. Values of Ro as of Table 1. The dotted lines indicate the critical value of the spanwise wavelength used to determine whether the VLSM is fully suppressed.

with the VLSM at the same spanwise wavelengths. Indeed, spectral energy content is still observable in the (co)-spectra at $\lambda_z/h = 5$ after the suppression of the VLSM, ensuring smoothness of the spectra. This would not be the case if modal damping were used, as all energy at large wavelengths would be removed yielding a discontinuous spectrum; similarly, if one were to restrict the spanwise simulation domain, large wavelengths would be unrepresentable (see de Giovanetti et al., 2016).

The spectrum $\boldsymbol{\Phi}_{uu}$ of streamwise fluctuations of Fig. 4(a,e) is re-analysed in the outer layer (at $y/h = 1$, more precisely) for all available simulations in Fig. 5. The peak associated to the VLSM is sharp, indicating that the VLSM is rather monochrome — meaning that its spectral representation mainly involves one or two Fourier modes only. By comparing the spectra of uncontrolled simulations (dashed lines) at low and high Reynolds number (panels a and b respectively), the Reynolds number dependence of the patterns of high- and low-speed streaks composing the VLSM can be appreciated. Even when scaling it in outer units, the energy associated to the pattern significantly increases with Reynolds number; moreover, its characteristic spanwise wavelength shifts from $\lambda_z/h \approx 3-4$ to a larger value of $\lambda_z/h \approx 5$, meaning that the pattern becomes larger in physical terms. This behaviour is expected and can also be observed in the data of Lee and Moser (2018).

As for the dependence on the rotation number at constant flow rate, the sharp spectral peak associated to the VLSM disappears already at the lowest value of Ro tested here — as far as the high-Re dataset is concerned (Fig. 5b). We interpret this as the VLSM being suppressed. The VLSM-peak is replaced by a weaker, smooth one, which shrinks in size and intensity as Ro further increases. At the lower Reynolds number (Fig. 5a), instead, the sharp energy peak progressively shrinks in size and intensity until it becomes smooth; determining the critical value of Ro for which the VLSM is fully suppressed is thus an arbitrary process, as no clear saturation effect is seen. This arbitrarity constitutes the main drawback of using the Coriolis force instead of other VLSM-suppressing strategies.

The critical value of Ro could be defined, for instance, as the one of minimum absolute value for which no sharp spectral peak is observed; the underlying argument would be that the VLSM is associated to a sharp spectral peak, as discussed before, whereas the spectral contributions of non-VLSM large scales are instead broadband. Alternatively, one can analyse the λ_z-position of the large-scaled outer-layer spectral peak seen in Fig. 5(a–b). The critical value of the rotation number could be defined as the one of minimum absolute value for which the outer-layer maximum of the power spectral density of u-fluctuations falls at a wavelength that is smaller than a given threshold. In Andreolli et al.

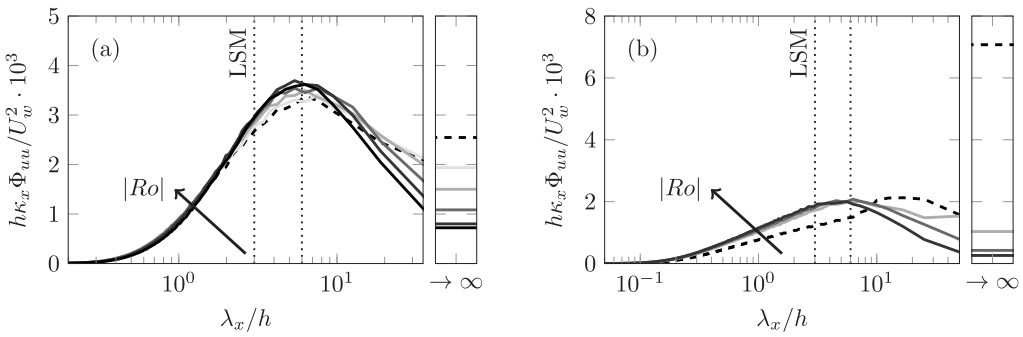

Fig. 6. Premultiplied one-dimensional streamwise spectrum $\kappa_x\Phi_{uu}$ of the streamwise fluctuations for changing value of the control intensity $|Ro|$ at the midplane ($y/h = 1$). Line styles as of Fig. 5; (a) $Re_\tau \approx 100$, (b) $Re_\tau \approx 500$. To the right of each panel, the value of the spectrum at $\lambda_x \to \infty$ is shown; such a value is premultiplied with the Fourier resolution $\Delta\kappa_x$ of our simulations. Two vertical dotted lines indicate the expected streamwise periodicity of LSMs ($\lambda_x/h = 3$) and the approximate wavelength ($\lambda_x/h \approx 6$) at which a maximum of the spectrum is seen for most of the present simulations.

(2021), we chose $\lambda_z/h \geq \pi$ as a suited criterion to discriminate the VLSM from the remaining scales of motions; owing to the discrete mesh used, this can be rewritten as $\lambda_z/h > 0.889\pi$ and $\lambda_z/h > 0.941\pi$ for the simulations at the low and high Reynolds numbers respectively. These values are used in this paper as the threshold defining the VLSM, and are shown in Fig. 5(a–b) as dotted lines.

These two methods both return the same value $Ro = -0.01$ for the low-Re dataset. As previously discussed, at high Reynolds number we consider the VLSM to be suppressed already at the lowest tested value of the rotation number ($Ro = -0.005$), although analysing the wavelength of maximum outer-layer spectral energy suggests a critical value of $Ro = -0.01$. The previous estimate based on visual inspection is deemed more credible, as the spectrum is substantially changed by increasing the magnitude of the rotation number from $Ro = 0$ to $Ro = -0.005$, whereas a further increase to $Ro = -0.01$ only leads to marginal changes. In other words, it seems that most of the VLSM-suppression has already taken place at $Ro = -0.005$ at high Reynolds number.

It appears, then, that the critical value of Ro at which the VLSM is fully suppressed decreases with Reynolds number. This is unsurprising. The rotation number is equal to (twice) the angular velocity Ω scaled in outer units, and it multiplies the flow velocity to yield the Coriolis acceleration. The magnitude of large-scale velocity fluctuations increases with Re even if scaling in outer units (see Fig. 5a,b; notice the different scale for the y-axis). Hence, the magnitude of the Coriolis force acting on large scales will increase with Re even if one keeps the angular velocity constant in outer units (that is, $Ro = const.$). In other words, it is reasonable to expect the same value of Ro to produce larger effects at a larger Reynolds number, as is here observed. Nonetheless, the data produced for this study is rather limited for a discussion of Reynolds number effects; further investigation is needed.

So far, we have only scrutinised spanwise velocity spectra. While these clearly identify the VLSM, they do not contain information about the streamwise extent of the turbulent structures. To recover this kind of information, Fig. 6 shows the premultiplied streamwise spectra of streamwise fluctuations for all available simulations. Data is shown at the centreline, where the Coriolis force has its strongest effects. Next to each panel, the value of the spectrum for $\lambda_x \to \infty$ (where λ_x is the streamwise wavelength) is shown; notice that the Fourier resolution $\Delta\kappa_x$ of the simulations is used for premultiplication in this case, as using the wavenumber $\kappa_x = 2\pi/\lambda_x = 0$ would hide the energy content of the spectrum. Such a value of the spectrum represents the energy contained in all streamwise-invariant Fourier modes or, in other words, the energy held by streamwise-invariant vortices. Although it is usually not shown, the energy of streamwise-invariant vortices is surprisingly high in the uncontrolled simulations of the present dataset, both at the lower (a) and especially at the higher (b) Reynolds number. We interpret this observation as follows. Despite being sufficiently wide in the spanwise direction, the simulation box used for the present study is too short in the streamwise one to correctly capture the extent of the VLSM: the latter is thus misrepresented as a streamwise-invariant vortex. In other words, most of the energy of the VLSM is contained on streamwise-invariant Fourier modes. Unlike in spanwise spectra (Fig. 5), no particularly pronounced sharp spectral peak is observed for finite values of the streamwise wavelength λ_x in Fig. 6, which reinforces our interpretation. Similar conclusions were drawn by Lee and Moser (2018) upon inspecting streamwise spectra in a much longer domain at $Re_\tau \approx 500$; the authors also note that the streamwise coherence length of the VLSM at $Re_\tau \approx 500$ exceeds $310h$. Correctly capturing the streamwise extent of such a long structure in a direct numerical simulation is prohibitively expensive.

What is also surprising about the streamwise spectra of Fig. 6 is the lack of an expected feature. Typically, a spectral peak associated to LSMs is observed at $\lambda_x/h = 3$; it is observed in channel, pipe and boundary layer flows (Monty et al., 2009). We do not observe it here in any of our simulations, including the uncontrolled ones. At the lower Reynolds number (Fig. 6a), a spectral peak is seen at around $\lambda_x/h \approx 6$ in the uncontrolled simulation; at the higher one (b), the peak is seen around $\lambda_x/h \approx 20$. Perhaps, all outer-scaled eddies have a larger extent in Couette flows as they have in other wall-bounded flows; following this interpretation, then, the spectral peaks seen at $\lambda_x/h \approx 6$ and $\lambda_x/h \approx 20$ at $Re_\tau \approx 100$ and $Re_\tau \approx 500$ respectively would represent the LSMs of the considered Couette flows. The typical rolling motion, which is much larger in extent and is represented as streamwise-invariant in our simulation, would instead constitute the very-large-scale motion of a Couette flow, consistently with the nomenclature used in this paper. It is also possible, however, that such a categorisation of outer-scaled motions into LSMs and VLSMs simply does not apply to Couette flows. An in-depth discussion of the matter is out of the scope of the present paper and is left for future work.

As for the effects of the Coriolis force on streamwise spectra, larger absolute values of the rotation number $|Ro|$ are associated to a reduction of the energy of streamwise-invariant vortices. This reinforces the idea that most of the energy of the VLSM is contained on streamwise-invariant Fourier modes, and that the VLSM is getting suppressed. A reduction of spectral content is also seen for the largest wavelengths represented in our simulations ($\lambda_x \approx 50$). Instead, motions of wavelength $\lambda_x/h \approx 6$ are energised by applying the Coriolis force both at the lower and higher Reynolds numbers. By combining this information with the one provided by spanwise spectra (see Figs. 4 and 5), we conclude that the control force considered here energises outer-scaled motions that are shorter and narrower than the suppressed VLSM.

While we observe that the main effect of a weak Coriolis force is to suppress the VLSM and energise some other outer-scaled eddies, effects on small scales cannot be excluded a-priori. Indeed, it is known that a strong enough rotation can also suppress small-scale turbulence (Tsukahara et al., 2010). Kline et al. (1967) suggested that the rotation might prevent small-scale low-speed streaks from being lifted up from the

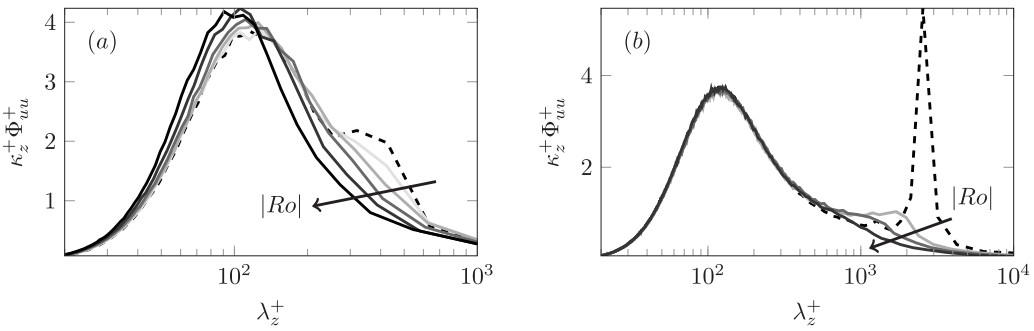

Fig. 7. Inner-scaled premultiplied one-dimensional spanwise spectrum $\kappa_z \Phi_{uu}$ of the streamwise fluctuations for changing value of the control intensity $|Ro|$ at $y^+ = 12$; (a) $Re_\tau \approx 100$ and (b) $Re_\tau \approx 500$. Line styles as of Fig. 5.

wall, halting turbulence-producing events. Therefore, we discuss the effects of the Coriolis force on small scales by analysing the spectrum Φ_{uu} of streamwise fluctuations in the near-wall region at $y^+ = 12$. This is done in Fig. 7, once again for all available simulations. The wall-normal position is chosen to match the one at which the maximum of the near-wall fluctuation energy is seen. The near-wall footprint of the VLSM is clearly observable both at low (a) and high (b) Reynolds number in the uncontrolled setting (dashed line). As the control intensity increases, the footprint gradually vanishes as expected. As for the small-scale peak at $\lambda_z^+ \approx 100$, its inner-scaled intensity and the wavelength at which it occurs are unaltered by the Coriolis force at high Reynolds number, as seen in panel (b). This observation matches the expected universal scaling in viscous units of the small-scale peak (Marusic et al., 2010), suggesting that the effect of a weak Coriolis force on the small scales is negligible. On the contrary, at the lower Reynolds number, the spectra of the controlled cases do not collapse on the one of the uncontrolled simulation, not even for small values of λ_z^+. A separate analysis, not shown for brevity, indicates that the streak spacing (as measured by the λ_z-position of the small-scale spectral maximum; this is conceptually similar to, but differs slightly from, using the minimum of the velocity autocorrelation for this estimate, as done in Kim et al., 1987) decreases, whereas the peak intensity is increased. At the critical value of Ro previously determined ($Ro = -0.01$), the maximum small-scale value of the Φ_{uu} spectrum is 8% larger than in the reference case, and the streak spacing is reduced by 3.5%.

Owing to the nonlinearity of turbulent phenomena, the observed increase in small-scale energy at low Re could be linked to distortions in nonlinear large-small interactions that arise as large scales are suppressed (de Giovanetti et al., 2016). High-Re data indicates instead that small-scales are only minimally affected by the Coriolis force for the weak rotations here investigated. We conjecture that this difference is due to scale separation: at the lower Reynolds number (Fig. 7a), the small- and large-scale spectral peaks are much closer together than they are at high-Re (b).

3.2. The CPI framework and the FIK identity

A framework for the analysis of flow control strategies based on integral energy budgets was first introduced by Gatti et al. (2018). Later, it was generalised in Andreolli et al. (2021) to be applicable to Couette flows and to discriminate turbulent eddies of different scales. In the following, the more general formulation provided in the latter publication will be used; the framework will be referred to as the CPI framework (shorthand for Constant Power Input). It will be briefly re-discussed in this section and later used in Section 3.3 to analyse the present dataset. Notice that, although the CPI framework was indeed developed to assess the effect of different control strategies on flows sharing the same input power, it will be here applied to a dataset of simulations carried out at a Constant Flow Rate (CFR). This application is valid as the framework will not be used to measure drag reduction, but rather to gain physical insights on the processes through which drag reduction is achieved.

According to the CPI framework, the input power (per unit wet area) Π_t provided to a turbulent plane Couette or Poiseuille of a given flow rate flow is either spent as laminar dissipation Φ^L (corresponding to the theoretic minimum power per unit wet area needed to achieve such a flow rate) or as an overhead expense $\mathcal{P}^L$ caused by the presence of turbulence:

$$\Pi_t = \Phi^L + \mathcal{P}^L. \tag{5}$$

Keep in mind that the power input Π_t is the product of the wall shear stress and some characteristic velocity, that is $\Pi_t = \tau_w U_w$ in a Couette flow and $\Pi_t = \tau_w U_b$ in a Poiseuille one, U_b being the bulk velocity. The energy fluxes Φ^L and $\mathcal{P}^L$ are defined as

$$\Phi^L = \int_0^h \mu \left(\frac{\mathrm{d}U^L}{\mathrm{d}y}\right)^2 \mathrm{d}y, \tag{6}$$

$$\mathcal{P}^L = \int_0^h -\rho \langle u'v' \rangle \frac{\mathrm{d}U^L}{\mathrm{d}y}\, \mathrm{d}y, \tag{7}$$

where μ is the dynamic viscosity and U^L is the laminar velocity profile that achieves the same flow rate as the considered turbulent flow (see Gatti et al., 2018). If a Poiseuille flow is considered and Eq. (5) is made non-dimensional with $\frac{1}{2}\rho U_b^3$, the FIK identity (Fukagata et al., 2002) is obtained:

$$\frac{\tau_w U_b}{\rho U_b^3/2} = \frac{1}{\rho U_b^3/2}\int_0^h \mu \left(\frac{\mathrm{d}U^L}{\mathrm{d}y}\right)^2 \mathrm{d}y + \frac{1}{\rho U_b^3/2}\int_0^h -\rho \langle u'v' \rangle \frac{\mathrm{d}U^L}{\mathrm{d}y}\, \mathrm{d}y \tag{8}$$

$$C_f = \frac{6}{\rho h U_b/\mu} + 6\int_0^1 -\frac{\langle u'v' \rangle}{U_b^2}\left(1 - \frac{y}{h}\right) \mathrm{d}\left(\frac{y}{h}\right) \tag{9}$$

where $C_f = 2\tau_w/(\rho U_b^2)$. That is, Eq. (5) is exactly the same as the FIK identity, except for a factor; indeed, it represents an expression for the non-dimensional input power, whereas the FIK identity is an expression for the non-dimensional wall-shear stress. In particular, $\mathcal{P}^L$ is the direct analogous of the integral of the Reynolds shear stress appearing in the FIK identity (Eq. (9)). The CPI framework differs from the FIK identity in that the turbulent overhead $\mathcal{P}^L$ is further decomposed into an expense ϵ (turbulent dissipation) directly caused by turbulent fluctuations and an expense Φ^Δ (deviation dissipation) which is indirectly caused by turbulence by inducing distortions of the mean velocity profile,

$$\mathcal{P}^L = \Phi^\Delta + \epsilon. \tag{10}$$

As discussed in Section 1, the FIK identity has been used to estimate the share of skin friction for which the large scales are responsible. Usually de Giovanetti et al. (2016) and Agostini and Leschziner (2018),

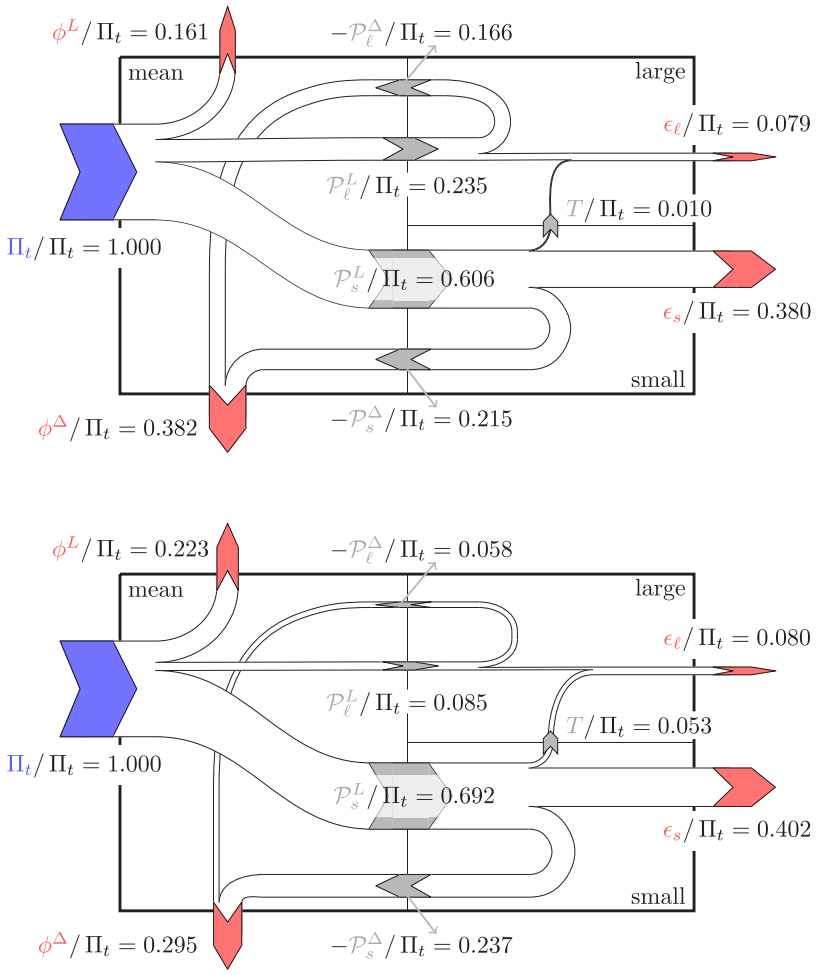

Fig. 8. Scale-decomposed energy box (Andreolli et al., 2021) for two Couette flows at $Re_\tau \approx 100$: no control (top), $Ro = -0.03$ (bottom).

the Reynolds shear stress $\langle u'v' \rangle$ is split into its small-scale and large-scale contributions, $\langle u'v' \rangle = \langle u'v' \rangle_s + \langle u'v' \rangle_\ell$. This enables then to calculate the contribution of small and large scales to C_f through the integral term in Eq. (9). Owing to the previous discussion, this procedure is exactly equivalent to calculating a small- and large-scale contribution to the turbulent overhead $\mathcal{P}^L$ ($\mathcal{P}^L_s$ and $\mathcal{P}^L_\ell$ respectively) as done in Andreolli et al. (2021). However, $\mathcal{P}^L_s$ and $\mathcal{P}^L_\ell$ do not exactly correspond to the energy losses caused by small and large fluctuations. In the following, we will motivate this statement with the help of the energy box introduced by Quadrio (2011) and later reworwked by Gatti et al. (2018) and Andreolli et al. (2021) to distinguish small and large fluctuations.

The energy box graphically represents how the input power Π_t is redistributed among the mean flow, small-scale fluctuations and large-scale ones. As an example, Fig. 8 shows the energy box for two flows considered in this paper, with and without Coriolis force. Notice that the Coriolis force does not exchange work with the flow (see Section 2), so that no power input associated to the control force needs to be added to the energy box. Although it is already clear from Fig. 8 that the Coriolis force disproportionately affects energy fluxes to and from large scales, a thorough discussion of its effect is given later in Section 3.3. The power input Π_t is supplied to the mean flow by some external agent; the mean flow is represented by the left part of the box, whereas the large and small fluctuations are represented to the right. Part of Π_t is directly dissipated by the mean flow as Φ^L, whereas the remaining part is passed to the small- and large-scale fluctuations through $\mathcal{P}^L_s$ and $\mathcal{P}^L_\ell$ respectively. Small- and large-scale fluctuations then exchange power through the cross-talk term T. Alternatively, they dissipate the received power either directly as turbulent dissipation ($\epsilon = \epsilon_s + \epsilon_\ell$) or indirectly by feeding it back to the mean flow through the deviation production ($\mathcal{P}^\Delta = \mathcal{P}^\Delta_s + \mathcal{P}^\Delta_\ell$; notice that $\mathcal{P}^\Delta < 0$). The entirety of deviation production is then lost as deviation dissipation, $\Phi^\Delta = -\mathcal{P}^\Delta$. Hence, small- and large-scale contributions to $\mathcal{P}^\Delta$ can be regarded as small- and large-scale contributions to the deviation dissipation Φ^Δ, which we define as follows:

$$\Phi^\Delta_s = -\mathcal{P}^\Delta_s, \qquad \Phi^\Delta_\ell = -\mathcal{P}^\Delta_\ell.$$

Using this notation, the integral turbulent kinetic energy balance for small- and large-scale fluctuations depicted in Fig. 8 can be written as:

$$\mathcal{P}^L_s = \Phi^\Delta_s + \epsilon_s + T, \tag{11}$$

$$\mathcal{P}^L_\ell = \Phi^\Delta_\ell + \epsilon_\ell - T. \tag{12}$$

It is clear from the above equation that $\mathcal{P}^L_\ell$ does not exactly represent the total dissipation $\Phi^\Delta_\ell + \epsilon_\ell$ caused by large scales, as it needs to be corrected by considering the inter-scale power transfer T. Similarly, the large-scale contribution to the integral term of Eq. (9) (which directly corresponds to $\mathcal{P}^L_\ell$) does not exactly quantify the large-scale contribution to the wall shear stress. The magnitude of the cross-talk term T is usually one order of magnitude smaller than the one of $\mathcal{P}^L_\ell$ and has a positive sign at low Reynolds number, meaning that a net power transfer from small to large scales is globally seen. By using $\mathcal{P}^L_\ell$ instead of $\Phi^\Delta_\ell + \epsilon_\ell$, then, the share of power wasted by large scales (or, equivalently, the large-scale contribution to τ_w if using the FIK method) is underestimated. As the Reynolds number increases, T changes in sign (meaning that an usual energy cascade from large to small scales is

Table 2
Share of the total power input Π_t that is dissipated by large scales in absence of control ($Ro = 0$), quantified either using $\Phi^{\Delta}_{\ell} + \epsilon_{\ell}$ (exact method) or $\mathcal{P}^{L}_{\ell}$. The second method is equivalent to calculating the effect of the large scales on the skin friction using the large-scale contribution to the integral term of the FIK identity (see Eq. (9)).
Source: Data from Andreolli et al. (2021).

	Using $\Phi^{\Delta}_{\ell} + \epsilon_{\ell}$ (exact)	Using $\mathcal{P}^{L}_{\ell}$ (equivalent to FIK)
$Re_\tau \approx 100$	24.5%	23.5%
$Re_\tau \approx 500$	38%	43.2%

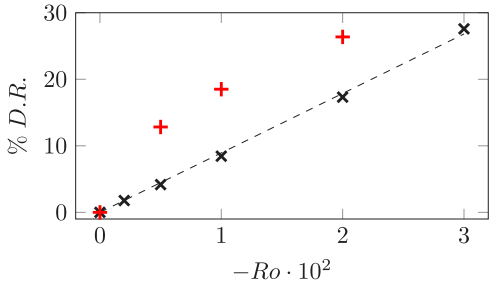

Fig. 9. Percentage drag reduction (% *D.R.*) obtained by applying the Coriolis force associated to a rotation number Ro at CFR; $Re_\tau \approx 100$ (black, ×) and $Re_\tau \approx 500$ (red, +). The black, dashed line indicates a linear fit for the low-Re data.

seen) and increases in magnitude, so that using $\mathcal{P}^{L}_{\ell}$ might result in a modest overestimation of the effect of large scales.

As an example, the data of Andreolli et al. (2021) is used to compare these two different ways of accounting for the power dissipated by large scales; results are shown in Table 2. Owing to the analogy with the FIK identity, these values also represent the contribution of large scales to the skin friction; they can also be interpreted as an upper bound for the drag-reduction achievable by the suppression of large scales.

3.3. Drag reduction

The drag reduction obtained by applying a Coriolis force with a given rotation number Ro at constant flow rate (CFR, $Re_w = const.$) is calculated using the friction Reynolds number $Re_\tau(Ro; Re_w)$ observed at that rotation number:

$$D.R.(Ro; Re_w) = 1 - \frac{Re^2_\tau(Ro; Re_w)}{Re^2_\tau(0; Re_w)}. \tag{13}$$

Results are shown in Fig. 9 for both the lower and higher Reynolds number datasets. For the low-Re dataset, the obtained drag reduction increases linearly with the control intensity ($-Ro$); the same cannot be said at high Reynolds number. While no saturation effect is seen at low-Re, high-Re data reveals that the gains in performance obtained by an increase of $|Ro|$ decrease with $|Ro|$ itself. We interpret this behaviour as follows: for small absolute values of the rotation number, the VLSM is progressively suppressed, so that a slight increase of $|Ro|$ yields a significant increase in performance owing to the suppression. As the rotation number approaches larger magnitudes, most of the VLSM-energy has already been removed; any increase in performance mostly stems from the effect of the Coriolis force on the remaining scales of motion, hence the reduced improvements over an increase of $|Ro|$. This is confirmed by the trends of CPI-fluxes shown in Fig. 10, which are discussed below, and matches the observations made on the energy spectra (Section 3.1).

Although the process is imperfect, it was shown in Section 3.1 that the suppression of the VLSM is satisfactory for $Ro = -0.01$ and $Ro = -0.005$ at the lower and higher Reynolds numbers respectively. These values of Ro correspond to 8.44% drag reduction at low-Re (starting from a reference friction Reynolds number $Re_\tau \approx 100$) and 12.8% at high-Re ($Re_\tau \approx 500$). We consider these values of drag reduction to be a sensible estimate of the drag reduction achievable by suppressing the VLSM: the control force might be too intrusive for larger magnitudes of Ro, whereas for lower ones the VLSM is not fully suppressed. Both values lie well below the theoretical maximum drag reduction given in Table 2. One obvious reason for the mismatch is that the values given in Table 2 estimate the drag reduction achievable by removing all motions whose spanwise wavelength is larger than a given threshold, including the VLSM; the Coriolis force instead only suppresses the VLSM. Moreover, a similar mismatch in the predicted and observed drag reduction was reported by both Fukagata et al. (2010) and de Giovanetti et al. (2016). Both authors found the reason for the mismatch in an increased small-scale contribution to skin friction, which in turn they attribute to different causes. The former argued that a decrease in pressure fluctuations causes the energisation of small scales; the latter attributed it to altered scale interactions. While both authors resorted to the FIK identity for their theoretical predictions, which possibly over-estimates the contribution of large scales to the skin friction (see Section 3.2), we expect the error introduced in doing so to be rather small at the Reynolds numbers considered. We further investigate the matter with the help of the CPI framework.

Owing to the discussion in Section 3.2, an expression for the skin friction coefficient is given by:

$$C_f = \frac{2}{\rho U_w^3}\left(\Phi^L + \epsilon + \Phi^{\Delta}\right). \tag{14}$$

As the laminar dissipation Φ^L is constant at CFR by definition, only a reduction of the turbulent or deviation dissipation (ϵ and Φ^{Δ} respectively) can yield a reduction of skin friction. Both these terms, as well as their small- and large-scale contributions (which have been calculated using a spanwise threshold wavelength of $\lambda_{z,c} = \pi$ as in Andreolli et al., 2021), are plotted in Fig. 10 for both the high and low Reynolds number datasets for increasing magnitude of Ro. These energy fluxes are scaled with $\frac{1}{2}\rho U_w^3$, since the velocity U_w of the walls remains constant as the simulations are carried out at CFR. Doing so, a decrease of a non-dimensional flux is associated to a decrease of its dimensional value. Moreover, the so-scaled energy fluxes can be interpreted as contributions to the skin friction as of Eq. (14).

A decrease of both the total turbulent and deviation dissipation is observed. Since the VLSM is known to primarily contribute to the deviation dissipation Φ^{Δ} (Andreolli et al., 2021), substantial savings in terms of the large-scaled contribution Φ^{Δ}_{ℓ} are expected. These are indeed seen at both low and high Reynolds number (c,d), as the value of Φ^{Δ}_{ℓ} approaches zero with increasing magnitude of Ro. At the higher Reynolds number, the value of Φ^{Δ}_{ℓ} saturates fast towards a zero-value, coherently with the idea that the VLSM is already satisfactorily suppressed at $Ro = -0.005$ (see Section 3.1). This might also explain why the trend of drag reduction deviates from a linear one at high Reynolds number (see Fig. 9), as previously discussed. Savings in Φ^{Δ}_{ℓ} are partially compensated by an increase of the contribution Φ^{Δ}_{s} of smaller scales to deviation dissipation; this holds for all the considered values of Ro at high Reynolds number, and only for low magnitudes of Ro at low Reynolds number.

As for the turbulent dissipation, its large-scale contribution ϵ_ℓ is expectedly marginal in absence of control and is only slightly decreased by the Coriolis force. The latter causes a significant decrease of the small-scale dissipation ϵ_s instead. Such a decrease is expected, and can be interpreted as an indirect effect of the removal of the VLSM: its suppression indeed triggers a reduction of the wall shear stress, which is well known to govern the scaling of the small scales. Hence, a decrease of small scale activity is expected, including a decrease of their contribution ϵ_s to dissipation; this further reduces the wall shear stress. Despite their absolute reduction, though, the observed values of ϵ_s are higher than expected. It is indeed known (see Abe and Antonia, 2016) that the turbulent dissipation ϵ scales as $\rho u_\tau^3 \log(Re_\tau)$; the trend that would result if such a scaling were to hold when the Coriolis force is applied is shown in Fig. 10. As can be seen, the observed values of

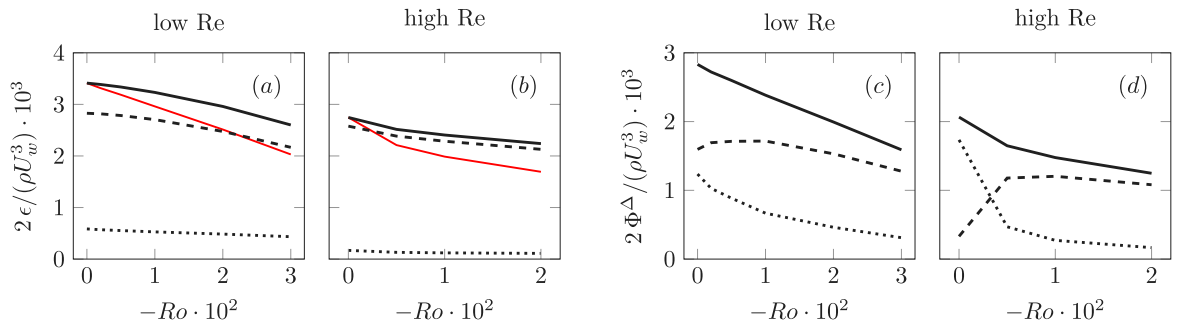

Fig. 10. Turbulence-induced dissipation terms scaled in outer units for changing control intensity $-Ro$ at CFR; turbulent dissipation ϵ (a,b) and deviation dissipation Φ^{Δ} (c,d) split into their small- (dashed) and large-scale components (dotted). (a), (c) $Re_\tau \approx 100$; (b), (d) $Re_\tau \approx 500$. The red, solid lines indicate the expected $\epsilon \sim \rho u_\tau^3 \log(Re_\tau)$ scaling. (For interpretation of the references to colour in this figure legend, the reader is referred to the web version of this article.)

ϵ exceed the expected ones. The excess dissipation can be attributed to ϵ_s, as the magnitude of ϵ_ℓ is negligible.

Both the trends of Φ_s^{Δ} and ϵ_s highlight that the drag reduction achieved by suppressing large scales is mitigated by a higher-than-expected contribution to skin friction from smaller scales. Notice that the threshold wavelength $\lambda_{z,c} = \pi$ used to separate large- and small-scale energy fluxes effectively separates the extremely large VLSM from the remaining scales of motion; in other words, Φ_s^{Δ} and ϵ_s receive contributions not only from inner-scaled eddies, but also from large, outer-scaled ones that are still smaller than the VLSM. The latter are, for instance, eddies whose spanwise wavelength falls in the range $1 \leq \lambda_z/h \leq \pi$; likely, they are responsible for the unexpectedly high values of Φ_s^{Δ} and ϵ_s. Indeed, the analysis of Section 3.1 has revealed that inner-scaled eddies hold the usual, viscous-scaling amount of energy even after the VLSM is suppressed. Instead, some outer-scaled motions located at the centreline (satisfying $1 \leq \lambda_z/h \leq \pi$) are energised by the Coriolis force, and this energisation possibly leads to increased values of the skin friction.

4. Discussion: the Coriolis force as a feedback control

We have so far shown that applying a Coriolis force to the flow achieves drag reduction by suppressing the VLSM. In this section, we argue that the Coriolis force functions in a way that resembles the feedback control proposed by Fukagata et al. (2005).

The Coriolis force $\vec{f}_c$ can be Reynolds-decomposed to yield its mean $\left\langle \vec{f}_c \right\rangle$ and fluctuating $\vec{f}_c'$ parts:

$$\vec{f}_c = -2\rho\,\Omega\hat{z}\times\vec{u} = \underbrace{-2\rho\,\Omega\hat{z}\times U\hat{x}}_{=\left\langle \vec{f}_c \right\rangle} + \underbrace{-2\rho\,\Omega\hat{z}\times\vec{u}'}_{=\vec{f}_c'}. \tag{15}$$

As U only depends on the wall normal coordinate y, so does the mean Coriolis force $\left\langle \vec{f}_c \right\rangle$; moreover, the only non-zero component of $\left\langle \vec{f}_c \right\rangle$ is the one in the wall-normal direction. Such a force field can be trivially shown to be conservative; as a consequence, its effect on the flow field is null, as it simply gets balanced by a static pressure gradient in the wall-normal direction. For the same reason, the Coriolis force has no impact on laminar flows (see Hide, 1977, sec. 2, lemma *iv*).

Hence, the VLSM-suppressing action must be provided by the fluctuating part $\vec{f}_c'$ of the force, which operates in the wall-normal and streamwise directions with magnitudes:

$$f_{c,x}' = \vec{f}_c' \cdot \hat{x} = -2\rho|\Omega|v' \tag{16}$$

$$f_{c,y}' = \vec{f}_c' \cdot \hat{y} = 2\rho|\Omega|u' \tag{17}$$

where the angular velocity has been rewritten as $\Omega = -|\Omega|$ for ease of reading; indeed, we only consider cyclonic rotations ($\Omega < 0$). To illustrate the action of the fluctuating part of the Coriolis force, we resort to the displaced-particle analysis shown in Tritton (1992). Consider a fluid particle at some wall-normal distance where the value of the mean velocity is U_1; U_1 is also the expected value of the streamwise velocity of the fluid particle. The particle is then displaced upwards by $\xi \to 0, \xi > 0$ over a time frame $\Delta t \to 0$ as an effect of an upwards velocity fluctuation, $v_*' > 0$, where $v_*' = \xi/\Delta t$. As this happens, the fluid particle is slowed down by the Coriolis force to reach a velocity U_* in its displaced position:

$$U_* = U_1 + \int_0^{\Delta t} \frac{f_{c,x}'}{\rho}\,\mathrm{d}t = U_1 + \int_0^{\Delta t} -2|\Omega|v_*'\,\mathrm{d}t \tag{18}$$

$$\approx U_1 - 2|\Omega|\xi. \tag{19}$$

At this new wall-normal position, the expected value of the velocity is $U_2 \approx U_1 + (dU/dy)\,\xi$, with $U_2 > U_1$ owing to the positive velocity gradient. Even in absence of a Coriolis force, the displaced particle would then induce a negative velocity fluctuation $-(dU/dy)\,\xi$; this can explain the negative sign of the Reynolds shear stress $\langle u'v' \rangle$. Additionally, the Coriolis force slows down the displaced particle as illustrated before, so that the observed velocity fluctuation u_*' reads:

$$u_*' = U_* - U_2 \approx -\left(2|\Omega| + \frac{\mathrm{d}U}{\mathrm{d}y}\right)\xi. \tag{20}$$

In other words, the streamwise component of the Coriolis force tends to increase the magnitude of the streamwise velocity fluctuations; this is however at odds with the observed stabilisation associated to the suppression of the VLSM. The stabilising effect is instead given by the wall-normal component of the Coriolis force fluctuation,

$$f_{c,y*}' = 2\rho|\Omega|u_*' \approx -2\rho|\Omega|\xi\left(2|\Omega| + \frac{\mathrm{d}U}{\mathrm{d}y}\right) < 0, \tag{21}$$

which is negative, hence it tends to return the displaced particle to its original position. The Coriolis force, then, interferes with the mechanism that produces the anti-correlation of u' and v' fluctuations — that is, it hinders the formation of a negative Reynolds shear stress.

The displaced particle analysis then indicates that the Coriolis force functions in a similar way to the feedback control of Fukagata et al. (2005), which is designed to directly weaken the Reynolds shear stress. Such a feedback control is exactly equivalent to the present Coriolis force deprived of its streamwise component, so that the control force only acts in the wall-normal direction with an intensity that is proportional to streamwise velocity fluctuations (see Eq. (17); notice that Fukagata et al., 2005, use a cylindrical coordinate system where the wall-normal axis points towards the wall, leading to an opposite sign of the control force with respect to the present manuscript). Streamwise velocity fluctuations are statistically associated to wall-normal fluctuations of opposite sign; the latter are opposed by both the Coriolis force and the feedback control of Fukagata et al. (2005), which deliver a wall-normal acceleration of the same sign as streamwise fluctuations. In this sense, both control strategies are analogous to an opposition control scheme; the obvious difference is that the sensing

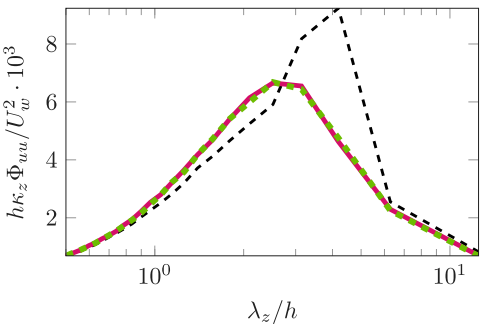

Fig. 11. Premultiplied one-dimensional spanwise spectrum $\kappa_z\Phi_{uu}$ of the streamwise fluctuations at $y/h = 1$ for the low Reynolds number dataset ($Re_\tau \approx 100$). The black dashed lines indicates the uncontrolled simulation ($Ro = 0$); the solid magenta line represents data with the usual Coriolis force and $Ro = -0.01$. For the green, dashed line, only the wall-normal component of the Coriolis force ($Ro = -0.01$) is retained; moreover, the stream- and span-wise average of the force is removed from it. (For interpretation of the references to colour in this figure legend, the reader is referred to the web version of this article.)

and the actuation for an opposition control is usually performed at the wall (eg. Abbassi et al., 2017), whereas the Coriolis force and the feedback control act at each point in the fluid domain.

To provide evidence in favour of the proposed analogy, we carry out an additional simulation at low Reynolds number and $Ro = -0.01$, where the streamwise and spanwise average of the Coriolis force as well as its streamwise component are removed. In other words, only the fluctuating part of the wall-normal component of the Coriolis force is retained, so as to effectively mimic the feedback control of Fukagata et al. (2005). Results are shown in Fig. 11, that compares the so-obtained one-dimensional spanwise spectrum of the streamwise fluctuations at $y/h = 1$ with the one of the corresponding simulations with and without Coriolis force. The modified Coriolis force is able to suppress the spectral peak associated to the VLSM and to closely replicate the velocity spectrum yielded by the standard Coriolis force, confirming our hypothesis.

Following Fukagata et al. (2005), we now proceed to show how the Coriolis force changes the budget equation of the Reynolds shear stress, as this may hint at why the force selectively suppresses the VLSM. To be precise, we inspect the co-spectrum $\boldsymbol{\Phi}_{uv}$ of the Reynolds shear stress. Its real part $\mathcal{R}e\left(\boldsymbol{\Phi}_{uv}\right)$ represents the contribution of each Fourier mode of wavenumber κ_z to $\langle u'v' \rangle$: it can be trivially shown (following e.g. Davidson, 2015, chapter 8) that

$$\left\langle u'v' \right\rangle = \int_{-\infty}^{\infty} \mathcal{R}e\left(\boldsymbol{\Phi}_{uv}\right) \, \mathrm{d}\kappa_z. \tag{22}$$

A budget equation for $\boldsymbol{\Phi}_{uv}$ is provided by Lee and Moser (2019); by adding the contribution of the Coriolis force and taking the real part of both sides of the equation, it can be written as:

$$\underbrace{\frac{\partial}{\partial t}\mathcal{R}e\left(\boldsymbol{\Phi}_{uv}\right)}_{\text{typically} < 0} = \mathcal{R}e\left(\text{RHS}\right) \underbrace{- 2|\Omega|\boldsymbol{\Phi}_{vv}}_{\text{cont. of } f'_{c,x}} + \underbrace{2|\Omega|\boldsymbol{\Phi}_{uu}}_{\text{cont. of } f'_{c,y}} \tag{23}$$

where RHS indicates all the terms normally appearing in the budget equation (not shown for brevity). The real part $\mathcal{R}e\left(\boldsymbol{\Phi}_{uv}\right)$ of the co-spectrum is typically negative, as is the Reynolds shear stress. The contributions of the streamwise and wall-normal components $f'_{c,x}$ and $f'_{c,y}$ of the Coriolis force are proportional to the spectra $\boldsymbol{\Phi}_{vv}$ and $\boldsymbol{\Phi}_{uu}$ of the streamwise and wall-normal normal Reynolds stresses respectively; both $\boldsymbol{\Phi}_{vv}$ and $\boldsymbol{\Phi}_{uu}$ are real, positive numbers and the latter is typically larger by roughly an order of magnitude (see Fig. 4). Hence the contribution of the Coriolis force to the right hand side of Eq. (23) is dominated by the wall-normal component $f'_{c,y}$ (as expected from the above analysis) and has a positive sign. That is, the Coriolis force results in a sink term for the budget of $\mathcal{R}e\left(\boldsymbol{\Phi}_{uv}\right)$ (as this last quantity is negative). We have once again shown that the Coriolis force acts to directly destroy the Reynolds shear stress like the feedback control of Fukagata et al. (2005) does.

Eq. (23) has further implications. In an uncontrolled setting, the spectrum $\boldsymbol{\Phi}_{uu}$ is maximum at the scale (i.e. wavenumber, or wavelength) of the VLSM, as shown by the spectrum of Fig. 4 (notice that the spectrum is premultiplied; values of the spectrum seen at large scales are effectively larger with respect to the ones at small scales than it appears from Fig. 4). Consequently, the application of a Coriolis force would primarily target the Reynolds shear stress at the scale of the VLSM. While the destruction of Reynolds shear stress clearly explains the observed drag reduction (as implied by Eq. (9)), explaining how energy at the VLSM-scale is removed from the normal Reynolds stresses is not as straightforward. Indeed, the direct effect of the Coriolis force on the streamwise and wall-normal spectra $\boldsymbol{\Phi}_{uu}$ and $\boldsymbol{\Phi}_{vv}$ is to transfer energy from the wall-normal to the streamwise one, as can be shown by writing a budget equation analogous to Eq. (23) (not shown for brevity). This is consistent with the fact that the Coriolis force does not exchange work with the flow (see Section 2). Most importantly, this direct effect cannot explain the destruction of energy at the VLSM-scale seen in Fig. 4.

Instead, the destruction of VLSM-energy must happen through an indirect mechanism. We have already argued that the Coriolis force directly suppresses the Reynolds shear stress at the VLSM-scale. The Reynolds shear stress is the intermediary through which $\langle u'u' \rangle$ receives energy from the mean flow (production of turbulent kinetic energy, see Davidson, 2015); a reduction of the shear stress at the VLSM-scale would likely result in a reduction of $\langle u'u' \rangle$-stresses at the same scale. The remaining contributions $\langle v'v' \rangle$ and $\langle w'w' \rangle$ to the kinetic energy do not receive energy from the mean flow in the present geometrical configuration; instead, the energy fed to streamwise fluctuations is redistributed to the remaining components by the pressure-rate-of-strain correlation (Davidson, 2015, chapter 4.4.1). It is then conceivable that the lack of $\langle u'u' \rangle$-energy at the VLSM-scale would result in lacking energy at the same scale on the other velocity components.

The mechanism described above is summarised in Fig. 12 and might explain how the VLSM is selectively suppressed by the Coriolis force. It has however its own limitations. For instance, once the VLSM is removed, the small scales would become the dominant feature of the $\boldsymbol{\Phi}_{uu}$ spectrum (at least in the near-wall region). Owing to the above discussion, then, the Coriolis force would proceed to destroy $\boldsymbol{\Phi}_{uv}$ at these scales — which does not happen for the limited values of Ro considered in this paper. Likely, the degree of suppression is determined by the relative magnitude of the contributions of the Coriolis force with respect to the terms labelled RHS in Eq. (23). Also, an alternative way of discussing the selective suppression of the VLSM would be to consider linear transient growth mechanisms. These lead to the amplification of flow structures that are comparable in size and topology to the small and outer-layer scales of wall turbulence (for instance, Del Álamo and Jiménez, 2006); it has been argued (Lozano-Durán et al., 2021) that the existence of these mechanisms is a sufficient condition for the formation of the typically observed structures. Perhaps, adding a Coriolis force to the flow selectively hinders the mechanisms leading to the amplification of outer-scaled motions, without much affecting smaller-scale mechanisms. The verification of this hypothesis is left for future research.

5. Conclusions

We have shown that a feedback control that exchanges no power with the flow is able to suppress the streamwise-elongated, outer-scaled rolling motion (the VLSM) typical of a turbulent Couette flow at a low to moderate Reynolds number using DNS. We argue that the control force works by directly suppressing the Reynolds shear stress $\langle u'v' \rangle$ at selected scales; in this sense, it resembles the feedback control of Fukagata et al. (2005).

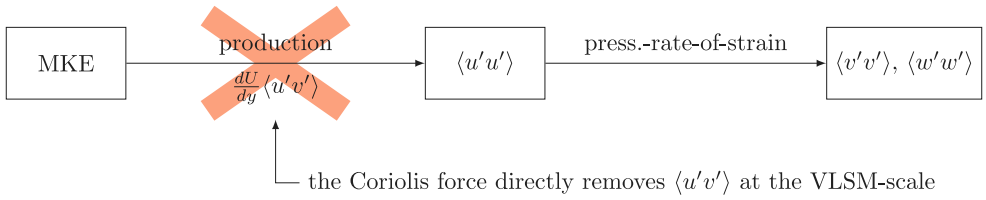

Fig. 12. Proposed mechanism for the selective suppression of the VLSM in Couette flows. The acronym MKE indicates the energy of the mean flow U (Mean Kinetic Energy). The Coriolis force directly suppresses $\langle u'v'\rangle$ at the scale of the VLSM. As a consequence, production of $\langle u'u'\rangle$ is stopped at such a scale; eventually, this will affect the formation of $\langle v'v'\rangle$ and $\langle w'w'\rangle$ energy too.

Using the CPI framework, which we have shown to be an extended and rescaled version of the FIK identity, the VLSM can be associated to costly distortions of the mean velocity profile (Andreolli et al., 2021); the share of power wasted in this way is referred to as deviation dissipation Φ^{Δ}. While large-scale contributions to Φ^{Δ} are greatly reduced by suppressing the VLSM (corroborating the previous statement), these gains in performance are hindered by a higher-than-expected contribution to Φ^{Δ} and to the turbulent dissipation ϵ by smaller (but not necessarily small) scales. This observation is coherent with previous similar works (Fukagata et al., 2010; de Giovanetti et al., 2016) and we attribute the unexpected skin friction contributions to the energisation of outer-scaled eddies that is observed as the VLSM is suppressed.

While the approach used here yields a progressive suppression of the VLSM, making it complicated to determine when the suppression is complete, a sensible estimate of the drag reduction achievable by targeting the VLSM is in the order of 8% starting from a reference friction Reynolds number $Re_\tau \approx 100$ and 13% for $Re_\tau \approx 500$. The latter value is higher than the drag reduction reported by de Giovanetti et al. (2016), who also performed a numerical experiment that suppressed outer-scaled motions in a channel flow. This discrepancy can be explained by differences in the suppressing strategy; most importantly, the above authors were considering a flow in which outer-scaled motions are weaker than in the Couette one considered here. However, since large scales are known to get more intense with the Reynolds number (Hutchins and Marusic, 2007b), higher values of drag reduction can be expected also in channel and boundary layer flows at a high Reynolds number. This is encouraging, as high Reynolds numbers are usually encountered in applications of industrial interest.

CRediT authorship contribution statement

A. Andreolli: Conceptualization, Software, Investigation, Formal analysis, Writing (Original Draft, Review & Editing), Project Administration. **M.K. Singh:** Software, Investigation, Data Curation, Visualization, Writing (Original Draft). **D. Gatti:** Conceptualization, Supervision, Funding Acquisition, Writing (Review & Editing).

Declaration of competing interest

The authors declare that they have no known competing financial interests or personal relationships that could have appeared to influence the work reported in this paper.

Data availability

Data will be made available on request.

Funding and acknowledgements

This work is supported by the Priority Programme SPP 1881 Turbulent Superstructures of the Deutsche Forschungsgemeinschaft (D.G. and A.A.; grant no. GA 2533/1-1).

The authors acknowledge support by the state of Baden-Württemberg through bwHPC. This work was performed with the help of the Large Scale Data Facility of the Karlsruhe Institute of Technology funded by the Ministry of Science, Research and the Arts Baden-Württemberg and by the German Federal Ministry of Education and Research.

References

Abbassi, M., Baars, W., Hutchins, N., Marusic, I., 2017. Skin-friction drag reduction in a high-Reynolds-number turbulent boundary layer via real-time control of large-scale structures. Int. J. Heat Fluid Flow 67, 30–41.

Abe, H., Antonia, R.A., 2016. Relationship between the energy dissipation function and the skin friction law in a turbulent channel flow. J. Fluid Mech. 798, 140–164.

Agostini, L., Leschziner, M., 2018. The impact of footprints of large-scale outer structures on the near-wall layer in the presence of drag-reducing spanwise wall motion. Flow Turbul. Combust. 100 (4), 1037–1061.

Agostini, L., Leschziner, M., 2019. The connection between the spectrum of turbulent scales and the skin-friction statistics in channel flow at $Re_\tau \approx 1000$. J. Fluid Mech. 871, 22–51.

Andreolli, A., Quadrio, M., Gatti, D., 2021. Global energy budgets in turbulent Couette and Poiseuille flows. J. Fluid Mech. 924, A25.

Baars, W.J., Marusic, I., 2020. Data-driven decomposition of the streamwise turbulence kinetic energy in boundary layers. Part 1. Energy spectra. J. Fluid Mech. 882, A25.

Balakumar, B., Adrian, R., 2007. Large- and very-large-scale motions in channel and boundary-layer flows. Phil. Trans. R. Soc. A 365 (1852), 665–681.

Bech, K.H., Andersson, H.I., 1996. Secondary flow in weakly rotating turbulent plane Couette flow. J. Fluid Mech. 317, 195–214.

Canton, J., Örlü, R., Chin, C., Hutchins, N., Monty, J., Schlatter, P., 2016a. On large-scale friction control in turbulent wall flow in low Reynolds number channels. Flow Turbul. Combust. 97 (3), 811–827.

Canton, J., Örlü, R., Chin, C., Schlatter, P., 2016b. Reynolds number dependence of large-scale friction control in turbulent channel flow. Phys. Rev. Fluids 1 (8), 081501.

Choi, H., Moin, P., Kim, J., 1994. Active turbulence control for drag reduction in wall-bounded flows. J. Fluid Mech. 262, 75–110.

Davidson, P., 2015. Turbulence: An Introduction for Scientists and Engineers, second ed. Oxford University Press.

de Giovanetti, M., Hwang, Y., Choi, H., 2016. Skin-friction generation by attached eddies in turbulent channel flow. J. Fluid Mech. 808, 511–538.

de Giovanetti, M., Sung, H.J., Hwang, Y., 2017. Streak instability in turbulent channel flow: The seeding mechanism of large-scale motions. J. Fluid Mech. 832, 483–513.

Deck, S., Renard, N., Laraufie, R., Weiss, P.-É., 2014. Large-scale contribution to mean wall shear stress in high-Reynolds-number flat-plate boundary layers up to $Re_\theta = 13650$. J. Fluid Mech. 743, 202–248.

Del Álamo, J.C., Jiménez, J., 2006. Linear energy amplification in turbulent channels. J. Fluid Mech. 559, 205.

Fukagata, K., Iwamoto, K., Kasagi, N., 2002. Contribution of Reynolds stress distribution to the skin friction in wall-bounded flows. Phys. Fluids 14 (11), L73–L76.

Fukagata, K., Kasagi, N., Sugiyama, K., 2005. Feedback control achieving sublaminar friction drag. In: Proceedings of the 6th Symposium on the Smart Control of Turbulence. pp. 143–148.

Fukagata, K., Kobayashi, M., Kasagi, N., 2010. On the friction drag reduction effect by a control of large-scale turbulent structures. J. Fluid Sci. Technol. 5 (3), 574–584.

Gandía-Barberá, S., Hoyas, S., Oberlack, M., Kraheberger, S., 2018. Letter: The link between the Reynolds shear stress and the large structures of turbulent Couette-Poiseuille flow. Phys. Fluids 30 (4), 041702.

Gatti, D., Cimarelli, A., Hasegawa, Y., Frohnapfel, B., Quadrio, M., 2018. Global energy fluxes in turbulent channels with flow control. J. Fluid Mech. 857, 345–373.

Gatti, D., Quadrio, M., 2016. Reynolds-number dependence of turbulent skin-friction drag reduction induced by spanwise forcing. J. Fluid Mech. 802, 553–582.

Hide, R., 1977. Experiments with rotating fluids. Q. J. R. Meteorol. Soc. 103 (435), 1–28.

Hoyas, S., Jiménez, J., 2006. Scaling of the velocity fluctuations in turbulent channels up to $Re_\tau = 2003$. Phys. Fluids 18 (1), 011702.

Hutchins, N., Marusic, I., 2007a. Evidence of very long meandering features in the logarithmic region of turbulent boundary layers. J. Fluid Mech. 579, 1–28.

Hutchins, N., Marusic, I., 2007b. Large-scale influences in near-wall turbulence. Phil. Trans. R. Soc. A 365 (1852), 647–664.

Hwang, Y., 2013. Near-wall turbulent fluctuations in the absence of wide outer motions. J. Fluid Mech. 723, 264–288.

Hwang, Y., 2015. Statistical structure of self-sustaining attached eddies in turbulent channel flow. J. Fluid Mech. 767, 254–289.

Hwang, Y., Cossu, C., 2010. Self-sustained process at large scales in turbulent channel flow. Phys. Rev. Lett. 105 (4), 044505.
Ibrahim, J.I., Guseva, A., Garcia-Mayoral, R., 2020. Selective opposition-like control of large-scale structures in wall-bounded turbulence. J. Phys. Conf. Ser. 1522 (1), 012015.
Illingworth, S.J., 2020. Streamwise-constant large-scale structures in Couette and Poiseuille flows. J. Fluid Mech. 889, A13.
Iwamoto, K., Fukagata, K., Kasagi, N., Suzuki, Y., 2005. Friction drag reduction achievable by near-wall turbulence manipulation at high Reynolds numbers. Phys. Fluids 17 (1), 011702–011702–4.
Iwamoto, K., Kasagi, N., Suzuki, Y., 2004. Dynamical roles of large-scale structures in turbulent channel flow. In: Computational Mechanics, WCCM VI in Conjunction with APCOM '04. In: MS022-174, Beijing, China, Sept. 5-10, 2004.
Jiménez, J., Moin, P., 1991. The minimal flow unit in near-wall turbulence. J. Fluid Mech. 225, 213–240.
Jiménez, J., Pinelli, A., 1999. The autonomous cycle of near-wall turbulence. J. Fluid Mech. 389, 335–359.
Johnston, J.P., Halleent, R.M., Lezius, D.K., 1972. Effects of spanwise rotation on the structure of two-dimensional fully developed turbulent channel flow. J. Fluid Mech. 56 (03), 533.
Karniadakis, G., Choi, K.-S., 2003. Mechanisms on transverse motions in turbulent wall flows. Annu. Rev. Fluid Mech. 35 (1), 45–62.
Kasagi, N., Suzuki, Y., Fukagata, K., 2009. Microelectromechanical systems–based feedback control of turbulence for skin friction reduction. Annu. Rev. Fluid Mech. 41 (1), 231–251.
Kawata, T., Alfredsson, P.H., 2016. Experiments in rotating plane Couette flow – momentum transport by coherent roll-cell structure and zero-absolute-vorticity state. J. Fluid Mech. 791, 191–213.
Kawata, T., Alfredsson, P.H., 2019. Scale interactions in turbulent rotating planar Couette flow: Insight through the Reynolds stress transport. J. Fluid Mech. 879, 255–295.
Kim, K.C., Adrian, R.J., 1999. Very large-scale motion in the outer layer. Phys. Fluids 11 (2), 417–422.
Kim, J., Moin, P., Moser, R., 1987. Turbulence statistics in fully developed channel flow at low Reynolds number. J. Fluid Mech. 177, 133–166.
Kline, S.J., Reynolds, W.C., Schraub, F.A., Runstadler, P.W., 1967. The structure of turbulent boundary layers. J. Fluid Mech. 30 (4), 741–773.
Komminaho, J., Lundbladh, A., Johansson, A.V., 1996. Very large structures in plane turbulent Couette flow. J. Fluid Mech. 320 (-1), 259.
Kristoffersen, R., Andersson, H.I., 1993. Direct simulations of low-Reynolds-number turbulent flow in a rotating channel. J. Fluid Mech. 256, 163–197.
Lee, M., Moser, R.D., 2018. Extreme-scale motions in turbulent plane Couette flows. J. Fluid Mech. 842, 128–145.
Lee, M., Moser, R.D., 2019. Spectral analysis of the budget equation in turbulent channel flows at high Reynolds number. J. Fluid Mech. 860, 886–938.
Lezius, D.K., Johnston, J.P., 1976. Roll-cell instabilities in rotating laminar and trubulent channel flows. J. Fluid Mech. 77 (1), 153–174.
Lozano-Durán, A., Constantinou, N.C., Nikolaidis, M.-A., Karp, M., 2021. Cause-and-effect of linear mechanisms sustaining wall turbulence. J. Fluid Mech. 914, A8.
Luchini, P., Quadrio, M., 2006. A low-cost parallel implementation of direct numerical simulation of wall turbulence. J. Comput. Phys. 211 (2), 551–571.
Marusic, I., Chandran, D., Rouhi, A., Fu, M.K., Wine, D., Holloway, B., Chung, D., Smits, A.J., 2021. An energy-efficient pathway to turbulent drag reduction. Nature Commun. 12 (1), 5805.
Marusic, I., Mathis, R., Hutchins, N., 2010. High Reynolds number effects in wall turbulence. Int. J. Heat Fluid Flow 31 (3), 418–428.
Marusic, I., Perry, A.E., 1995. A wall-wake model for the turbulence structure of boundary layers. Part 2. Further experimental support. J. Fluid Mech. 298, 389–407.
Monty, J.P., Hutchins, N., Ng, H.C.H., Marusic, I., Chong, M.S., 2009. A comparison of turbulent pipe, channel and boundary layer flows. J. Fluid Mech. 632, 431–442.
Panton, R.L., 2001. Overview of the self-sustaining mechanisms of wall turbulence. Prog. Aerosp. Sci. 37 (4), 341–383.
Pirozzoli, S., Bernardini, M., Orlandi, P., 2014. Turbulence statistics in Couette flow at high Reynolds number. J. Fluid Mech. 758, 327–343.
Puccioni, M., Calaf, M., Pardyjak, E.R., Hoch, S., Morrison, T.J., Perelet, A., Iungo, G.V., 2023. Identification of the energy contributions associated with wall-attached eddies and very-large-scale motions in the near-neutral atmospheric surface layer through wind LiDAR measurements. J. Fluid Mech. 955, A39.
Quadrio, M., 2011. Drag reduction in turbulent boundary layers by in-plane wall motion. Phil. Trans. R. Soc. A 369 (1940), 1428–1442.
Quadrio, M., Ricco, P., 2004. Critical assessment of turbulent drag reduction through spanwise wall oscillations. J. Fluid Mech. 521, 251–271.
Quadrio, M., Ricco, P., Viotti, C., 2009. Streamwise-travelling waves of spanwise wall velocity for turbulent drag reduction. J. Fluid Mech. 627, 161–178.
Renard, N., Deck, S., 2016. A theoretical decomposition of mean skin friction generation into physical phenomena across the boundary layer. J. Fluid Mech. 790, 339–367.
Schoppa, W., Hussain, F., 1998. A large-scale control strategy for drag reduction in turbulent boundary layers. Phys. Fluids 10 (5), 1049–1051.
Tillmark, N., Alfredsson, P.H., 1996. Experiments on rotating plane Couette flow. In: Advances in Turbulence VI, vol. 36, Springer Netherlands, Dordrecht, pp. 391–394.
Toh, S., Itano, T., 2005. Interaction between a large-scale structure and near-wall structures in channel flow. J. Fluid Mech. 524, 249–262.
Tritton, D.J., 1992. Stabilization and destabilization of turbulent shear flow in a rotating fluid. J. Fluid Mech. 241, 503–523.
Tsukahara, T., Tillmark, N., Alfredsson, P.H., 2010. Flow regimes in a plane Couette flow with system rotation. J. Fluid Mech. 648, 5–33.
Walsh, M.J., Sellers, W.L., McGinley, C.B., 1989. Riblet drag at flight conditions. J. Aircr. 26 (6), 570–575.
Yao, J., Chen, X., Thomas, F., Hussain, F., 2017. Large-scale control strategy for drag reduction in turbulent channel flows. Phys. Rev. Fluids 2 (6), 062601.
Zhou, J., Adrian, R.J., Balachandar, S., Kendall, T.M., 1999. Mechanisms for generating coherent packets of hairpin vortices in channel flow. J. Fluid Mech. 387, 353–396.
Zhou, Z., Xu, C.-X., Jiménez, J., 2022. Interaction between near-wall streaks and large-scale motions in turbulent channel flows. J. Fluid Mech. 940, A23.